remote sensing

Automated Delineation of Supraglacial Debris Cover Using Deep Learning and Multisource Remote Sensing Data

Saurabh Kaushik [1,2,3,*], Tejpal Singh[1,2], Anshuman Bhardwaj [4], P. K. Joshi [5,6] and Andreas J. Dietz [3]

1 Academy of Scientific and Innovative Research (AcSIR), Ghaziabad 201 002, India
2 CSIR-Central Scientific Instrument Organisation, Chandigarh 160 030, India
3 German Remote Sensing Data Center (DFD), German Aerospace Center (DLR), Muenchener Str. 20, 82234 Wessling, Germany
4 School of Geosciences, University of Aberdeen, Meston Building, King's College, Aberdeen AB24 3UE, United Kingdom
5 School of Environmental Sciences, Jawaharlal Nehru University, New Delhi 110 067, India
6 Special Centre for Disaster Research, Jawaharlal Nehru University, New Delhi 110 067, India
* Correspondence: saurabh21.kaushik@gmail.com, saurabh.kaushik@dlr.de

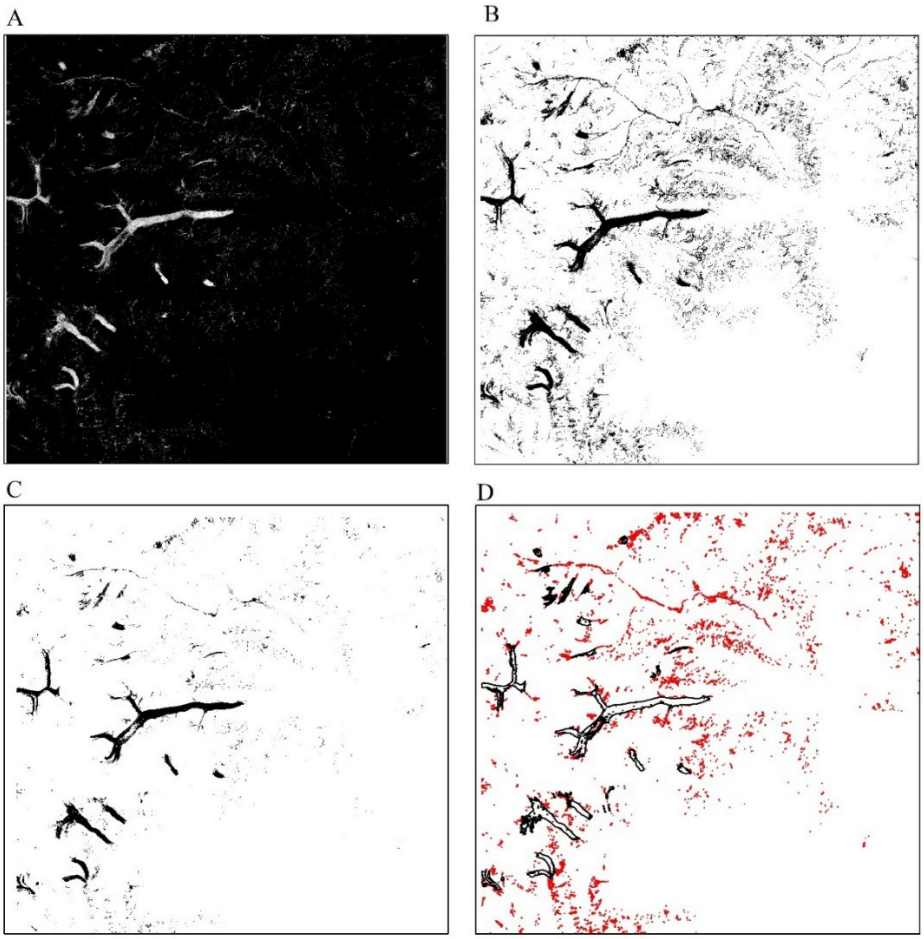

Figure S1. Illustration of the algorithm workflow and post-processing steps. (**A**) – results obtained via the proposed deep neural network (SGDNet), (**B**) – results obtained via the first post-processing step ($if\ DNN\ result > 0.3\ and\ elevation > 3300$), (**C**) – cleaning up of the result using a 5×5 median filter, and (**D**) – the results after vectorization, the red polygons (<0.02) are removed from the final results.

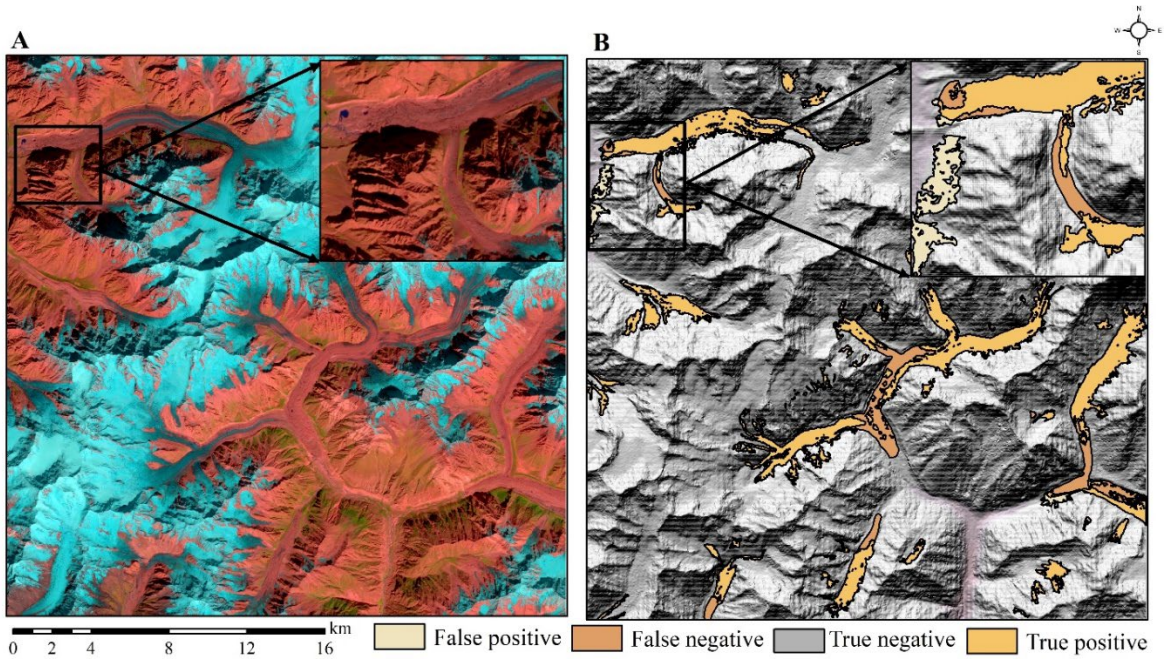

Figure S2. Impact of shadow on the classification accuracy of the proposed algorithm. A – presence of shadow in a satellite image, and B – classification of shadow as a false positive in the results obtained via the proposed algorithm.

Table S1. Data used in the present study.

Eastern Himalaya		
Satellite	**Scene ID/Product ID**	**Spatial resolution(m)**
Sentinel 1	S1A_IW_SLC__1SDV_20200410T235453_20200410T235520_032072_03B4CE_CFAF, S1A_IW_SLC__1SDV_20200422T235454_20200422T235521_032247_03BAF0_6F7D, S1A_IW_SLC__1SDV_20161115T000242_20161115T000312_013945_016754_A572, S1A_IW_SLC__1SDV_20170126T000239_20170126T000309_014995_0187CF_8AD1,	2.3 × 14.1
Sentinel 2	L1C_T45RXL_A007609_20161206T044556, L1C_T45RXL_A008324_20170125T044345, L1C_T46RBR_A019793_20201220T044209, L1C_T46RBS_A019793_20201220T044209,	VNIR – 10 SWIR - 20 VNIR (B1 & B9) – SWIR (B10) - 60
Landsat 8	LC81380402021003LGN00, LC81380412021003LGN00, LC81390412016365LGN01,	30, 15 PAN
ALOS DEM	AP_13363_FBS_F3050_RT1, AP_13363_FBS_F3060_RT1,	12.5
Central Himalaya		
Sentinel 1	S1A_IW_SLC_1SDV_20200402T001915_20200402T001942_031941_03B02B_E470, S1A_IW_SLC__1SDV_20200508T001917_20200508T001944_032466_03C281_2F01, S1A_IW_SLC__1SDV_20200515T001102_20200515T001130_032568_03C5AC_2086,	2.3 × 14.1

Sentinel 1	S1A_IW_SLC__1SDV_20200527T001103_20200527T001131_032743_03CAFC_D764, S1A_IW_SLC__1SDV_20200523T004312_20200523T004340_032685_03C929_4E86, S1A_IW_SLC__1SDV_20200511T004311_20200511T004339_032510_03C3DB_65FC	
Sentinel 2	L1C_T45RTM_A019021_20201027T050433, L1C_T45RTN_A019021_20201027T050433, L1C_T45RVM_A028673_20201218T045213, L1C_T45RVL_A028816_20201228T045214, L1C_T45RWL_A028816_20201228T045214, L1C_T45RWM_A028816_20201228T045214	VNIR – 10 SWIR - 20 VNIR (B1 & B9) – SWIR (B10) - 60
Landsat 8	LC81420402020301LGN00, LC81400412021001LGN00, LC81450382020274LGN00, LC81450392020274LGN00	30, 15 PAN
ALOS DEM	AP_05348_FBS_F0540_RT1, AP_05348_FBS_F0550_RT1, AP_07609_FBD_F0540_RT1, AP_07609_FBD_F0550_RT1, AP_08528_FBD_F0530_RT1, AP_08149_FBD_F0600_RT1, AP_08149_FBD_F0610_RT1, AP_08572_FBD_F0600_RT1	12.5
	Western Himalaya	
Sentinel 1	S1A_IW_SLC__1SDV_20200410T005051_20200410T005121_032058_03B45C_F131, S1A_IW_SLC__1SDV_20200422T005051_20200422T005121_032233_03BA7B_370F	2.3 × 14.1
Sentinel 2	L1C_T43SFS_A018335_20200909T054842, L1C_T43SFT_A018335_20200909T054842,	VNIR – 10 SWIR - 20 VNIR (B1 & B9) – SWIR (B10) - 60
Landsat 8	LC81470372020288LGN00, LC81480362020295LGN00, LC81480372020279LGN00,	30, 15 PAN
ALOS DEM	AP_07799_FBD_F0640_RT1, AP_07799_FBD_F0650_RT1 AP_07799_FBD_F0660_RT1 AP_08222_FBD_F0640_RT1 AP_08222_FBD_F0650_RT1 AP_08222_FBD_F0660_RT1	12.5
	Karakoram	
Sentinel 1	S1A_IW_SLC__1SDV_20200514T010617_20200514T010645_032554_03C53D_0763, S1A_IW_SLC__1SDV_20200526T010618_20200526T010646_032729_03CA8B_2515	
Sentinel 2	L1C_T43SCA_A018521_20200922T055400, L1C_T43SDA_A018521_20200922T055400,	VNIR – 10 SWIR - 20 VNIR (B1 & B9) – SWIR (B10) - 60

Landsat 8	LC81500352018255LGN00	30, 15 PAN
ALOS DEM	AP_05859_FBS_F0710_RT1, AP_05859_FBS_F0720_RT1, AP_05859_FBS_F0730_RT1, AP_07799_FBD_F0710_RT1, AP_07799_FBD_F0720_RT1, AP_07799_FBD_F0730_RT1, AP_08222_FBD_F0710_RT1, AP_08222_FBD_F0720_RT1, AP_12569_FBD_F0700_RT1, AP_12569_FBD_F0700_RT1, AP_12569_FBD_F0720_RT1	12.5

Table S2. Results of the various deep artificial neural network models used on the test data.

Hidden Layers	Activation Function	Optimizer	Learning Rate	Recall	Precision	F-Score
40-20-60	Relu	Adam	0.001	0.42	0.62	0.50
64-40-18	Relu	Adam	0.001	0.31	0.60	0.41
40-20-6	Relu	RMSprop	0.001	0.36	0.56	0.43
40-20-6	Tanh	Adam	0.001	0.70	0.68	0.69
40-20-5	Relu	Adam	0.001	0.38	0.62	0.47
60-30-15	Relu	Adam	0.001	0.31	0.60	0.41
128-62-30	Relu	Adam	0.001	0.32	0.64	0.43
40-80-60	Tanh	Adam	0.001	0.47	0.66	0.55
128-64-32	Tanh	Adam	0.001	0.69	0.75	0.72
256-128-64-32	Tanh	Adam	0.001	0.75	0.77	0.76
512—256-128-64-32	Tanh	Adam	0.0001	0.75	0.79	0.77
*1024-512—256-128-64-32	Tanh	Adam	0.0001	0.80	0.82	0.81

* The final used model